

This is the accepted manuscript made available via CHORUS. The article has been published as:

From two-dimensional spin vortex crystal to three-dimensional Néel order in the Mott insulator

$\text{Sr}_{2}\text{F}_{2}(\text{Fe}_{1-x}\text{Mn}_{x})_{2}\text{O}_{8}$

K. W. Bayliff, S. Wu, V. Loganathan, L. L. Zhao, J. K. Wang, Andriy H. Nevidomskyy, C.

Broholm, C.-L. Huang, and E. Morosan

Phys. Rev. B **99**, 024412 — Published 10 January 2019

DOI: [10.1103/PhysRevB.99.024412](https://doi.org/10.1103/PhysRevB.99.024412)

From 2D spin-vortex crystal to 3D Néel order in the Mott insulator $\text{Sr}_2\text{F}_2(\text{Fe}_{1-x}\text{Mn}_x)_2\text{OS}_2$

K. W. Bayliff

Department of Chemistry, Rice University, Houston, TX 77005, USA

S. Wu

*Institute for Quantum Matter and Department of Physics and Astronomy,
The Johns Hopkins University, Baltimore, MD 21218, USA and
Department of Physics, University of California Berkeley, Berkeley, CA 94720, USA*

V. Loganathan, L. L. Zhao, J. K. Wang, and Andriy H. Nevidomskyy

Department of Physics and Astronomy, Rice University, Houston, TX 77005, USA

C. Broholm

*Institute for Quantum Matter and Department of Physics and Astronomy,
The Johns Hopkins University, Baltimore, MD 21218, USA and
Neutron Scattering Division, Oak Ridge National Laboratory, Oak Ridge, TN 37831 USA*

C. -L. Huang and E. Morosan

Department of Physics and Astronomy, Rice University, Houston, TX 77005, USA

(Dated: November 15, 2018)

We report Mn and Co substitution at the Fe site in the tetragonal checkerboard Mott insulator $\text{Sr}_2\text{F}_2\text{Fe}_2\text{OS}_2$, which develops an antiferromagnetic two- \mathbf{k} spin vortex crystal at $T_N = 110$ K. While Co substitution increases T_N to 127 K ($x = 0.3$) in $\text{Sr}_2\text{F}_2(\text{Fe}_{1-x}\text{Co}_x)_2\text{OS}_2$, Mn substitution suppresses T_N for x up to 0.2 in $\text{Sr}_2\text{F}_2(\text{Fe}_{1-x}\text{Mn}_x)_2\text{OS}_2$ replacing the vortex crystal with a spin glass for $0.2 < x < 0.5$. The activation gap determined from resistivity has a local minimum of $E_g = 0.18$ eV for $x = 0.5$ where a new phase appears at $T_N = 45$ K. Neutron diffraction data along with corroborating magnetic evidence shows this is a G-type collinear antiferromagnet, with a transition temperature increasing for $0.5 < x < 0.8$. Density functional theory calculations point to the correlated nature of the transition metal d -bands: A modest Hubbard energy $U = 2$ eV is sufficient to open a Mott gap around the Fermi level. The calculations also correctly reproduce the ordered spin structure of $\text{Sr}_2\text{F}_2\text{Fe}_2\text{OS}_2$ and $\text{Sr}_2\text{F}_2\text{FeMnOS}_2$. A deeper understanding of the nature of the magnetic ordering is obtained within an effective theoretical model of local moments with doping-dependent competing exchange interactions $J_1 - J_2 - J'_2$.

I. INTRODUCTION

Understanding emergent properties of strongly interacting electrons often requires new materials and a new frame of reference. Topological spin textures are a case in point. Skyrmion crystals have been documented in non-centrosymmetric magnets with B20 structure (MnSi [?], $\text{Fe}_{1-x}\text{Co}_x\text{Si}$ [?], MnGe [?]) and in a Mott insulating multiferroic Cu_2OSeO_3 [?]. In these examples the Dzyaloshinski-Moriya interaction produces a helical spin structure, which transforms into a skyrmion crystal under the application of an external magnetic field. While skyrmions are hedgehog-like three-dimensional structures in spin space, a conceptually similar but simpler example of a topological defect is a spin vortex. Unlike the Abrikosov vortex crystals in type II superconductors that are stabilized by the orbital coupling to an external magnetic field, creating a crystal of spin vortices is not easy. The few theoretical proposals that exist require frustration in a Mott insulator to form multi- \mathbf{Q} magnetic order, which is then partially melted into a spin vortex lattice by application of a strong

magnetic field[?]. Another theoretical proposal, also based on multi- \mathbf{Q} magnetic ordering, has been made in the context of frustrated magnetism in certain families of hole-doped iron pnictides[?], recently corroborated experimentally in Ni-doped $\text{CaKFe}_4\text{As}_4$ [?]. The presence of conduction electrons in the latter example however makes the spin vortex structure more complicated to detect and manipulate. Here we report the discovery and exploration through experiments and theory, of a strongly interacting Mott insulator that can be driven through a quasi-two-dimensional spin vortex crystal phase through alloying.

Layered transition metal oxides have been a major focus of condensed matter research, especially after the discovery of high- T_c superconductivity in cuprates and iron pnictides. The family of oxychalcogenide compounds $\text{A}_2\text{T}_2\text{OX}_2$ ($\text{A} = \text{RO}, \text{SrF}, \text{BaF}, \text{Na}$; $\text{T} = \text{Mn}, \text{Fe}, \text{Co}$; $\text{X} = \text{S}, \text{Se}$) with checkerboard layers has raised intense interest for the unique crystal and magnetic structures as well as Mott insulating behavior. The first reported compounds in this family, $\text{La}_2\text{O}_3\text{Fe}_2\text{X}_2$ ($\text{X} = \text{S}, \text{Se}$)[?], crystallize with a layered tetragonal structure, consisting

of tetrahedral La_2O_2 layers and checkerboard-like sheets made of face sharing FeO_2X_4 octahedra. By replacing the La_2O_2 sheets with different types of spacer layers of the same 2+ valence or substituting Fe with other 3d metals, a number of compounds with similar structures have been synthesized, including $\text{La}_2\text{O}_3\text{Co}_2\text{Se}_2$,^{??} $\text{R}_2\text{O}_3\text{Mn}_2\text{Se}_2$ (R = La, Ce, Pr),^{???} $\text{R}_2\text{O}_3\text{Fe}_2\text{Se}_2$ (R = La-Sm),[?] $\text{A}_2\text{F}_2\text{T}_2\text{OX}_2$ (“22212”; A = Sr, Ba; T = Mn, Fe; X = S, Se)[?] and $\text{Na}_2\text{Fe}_2\text{OSe}_2$.[?] In spite of their structural similarity, neutron diffraction experiments have revealed a rich variety of magnetic structures in these compounds: While $\text{La}_2\text{O}_3\text{Mn}_2\text{Se}_2$ has a G-type antiferromagnetic (AFM) structure,[?] a bi-collinear AFM and a non-collinear plaquette AFM structure have been observed in its Fe[?] and Co[?] analogues, respectively. Our own study on $\text{Sr}_2\text{F}_2\text{Fe}_2\text{OS}_2$ has revealed a two-**Q** non-collinear AFM structure[?], which is similar to that of $\text{La}_2\text{O}_3\text{Co}_2\text{Se}_2$ [?] though with a sign change for a next nearest neighbor correlation. It is the presence of the two-**Q** magnetic ordering and the chemical flexibility that makes $\text{Sr}_2\text{F}_2\text{Fe}_2\text{OS}_2$ and its family of oxychalcogenides suitable for realizing topological spin structures.

From transport measurements and Density Functional Theory (DFT) calculations, there are indications of Mott insulating behavior in these oxychalcogenides, which is believed to be a result of the narrow transition metal 3d band.^{???} Consequently, these oxychalcogenides are of interest not only due to their potential for topological spin structures, but Mott insulators are also prime candidates to controllably tune their electronic properties toward the itinerant-to-local moment crossover, a regime known to give rise to strongly-correlated electron behavior or unconventional superconductivity. The fact that there are both cuprate and iron pnictide superconductors near the boundary between correlation-induced localization and itinerancy further motivates the present study of the oxychalcogenide family. While this type of electron delocalization has recently been realized in SmMnAsO ^{??} and LaMnOP [?] via doping and pressure tuning, the present study offers a first view of a four-component spin vortex crystal near the Mott transition.

We report tuning of the Mott insulating state in $\text{Sr}_2\text{F}_2\text{Fe}_2\text{OS}_2$ via Mn and Co substitution, showing non-monotonic variation of transport and thermodynamic properties. Our neutron diffraction and magnetic measurements demonstrate a change in the ground state spin structure induced by Mn doping, from a two-wavevector, non-collinear quasi-two-dimensional spin structure on the Fe-rich side, to a collinear three-dimensional, G-type AFM state with spins oriented along the c-axis on the Mn-rich side. Intermediate compositions show spin glass behavior indicative of competition between these two states. We analyze the origins of these two magnetic phases using a combination of DFT calculations and effective field

theory, demonstrating how the non-collinear structure in $\text{Sr}_2\text{F}_2\text{Fe}_2\text{OS}_2$ emerges from magnetic frustration. We show that this spin structure can be viewed as a checkerboard lattice of vortices and antivortices composed of Fe magnetic moments, and is a new type of topological *spin vortex crystal* analogous to, albeit with substantive differences with, those proposed in prior theoretical studies^{???}. Apart from a recently found realization of a similar spin structure in the biaxially ordered hole-doped iron pnictide $\text{CaKFe}_4\text{As}_4$ [?], $\text{Sr}_2\text{F}_2\text{Fe}_2\text{OS}_2$ studied here is, to the best of our knowledge, the only other magnet, and a first known Mott insulator, in which a spin vortex crystal has been proven to exist.

II. METHODS

Polycrystalline samples of $\text{Sr}_2\text{F}_2(\text{Fe}_{1-x}\text{Mn}_x)_2\text{OS}_2$ ($x = 0, 0.1, 0.15, 0.2, 0.3, 0.4, 0.5, 0.6, 0.7$) and $\text{Sr}_2\text{F}_2(\text{Fe}_{1-x}\text{Co}_x)_2\text{OS}_2$ ($x = 0.1, 0.2, 0.3$) were synthesized by solid state reaction, with SrF_2 , SrO , Fe , Mn or Co and S powders weighed and mixed in stoichiometric ratios inside a glovebox. The mixtures were then pressed into pellets, placed inside alumina crucibles, and sealed in quartz ampoules under partial argon pressure. The ampoules were heated to 800 °C at a rate of 50 °C/min, kept at that temperature for 24 hours, then slowly cooled to room temperature. The pellets were then ground, pelletized, and sealed again, followed by annealing at 850 °C to improve the sample quality and homogeneity. Attempts to synthesize compounds with higher dopant contents failed, as the solubility limits may have been reached in each respective system. Room temperature powder X-ray diffraction measurements were performed on a Rigaku D/Max diffractometer with Cu K_α radiation. The lattice parameters of each composition were determined from Rietveld refinements, using the RIETICA software package.

DC magnetization $M(T)$ was measured in a Quantum Design Magnetic Property Measurement System (QD MPMS), under both zero-field-cooled (ZFC) and field-cooled (FC) conditions. AC magnetization was measured on a QD Physical Property Measurement System (PPMS) with ACMS option. The scans were performed under zero DC field and an AC excitation field of 5 Oe, with various AC frequencies ranging from 500 to 10000 Hz. DC resistivity measurements were performed in a QD PPMS using a standard four-probe method. The data were acquired during both cooling and warming processes, showing no visible thermal irreversibility. Heat capacity measurements were performed in a QD PPMS using a thermal relaxation technique. Both resistivity and heat capacity measurements were carried out under zero magnetic field.

We performed DFT calculations of the electronic structure and magnetic properties in $\text{Sr}_2\text{F}_2\text{Fe}_2\text{OS}_2$ and $\text{Sr}_2\text{F}_2\text{FeMnOS}_2$. The full-potential linearized augmented

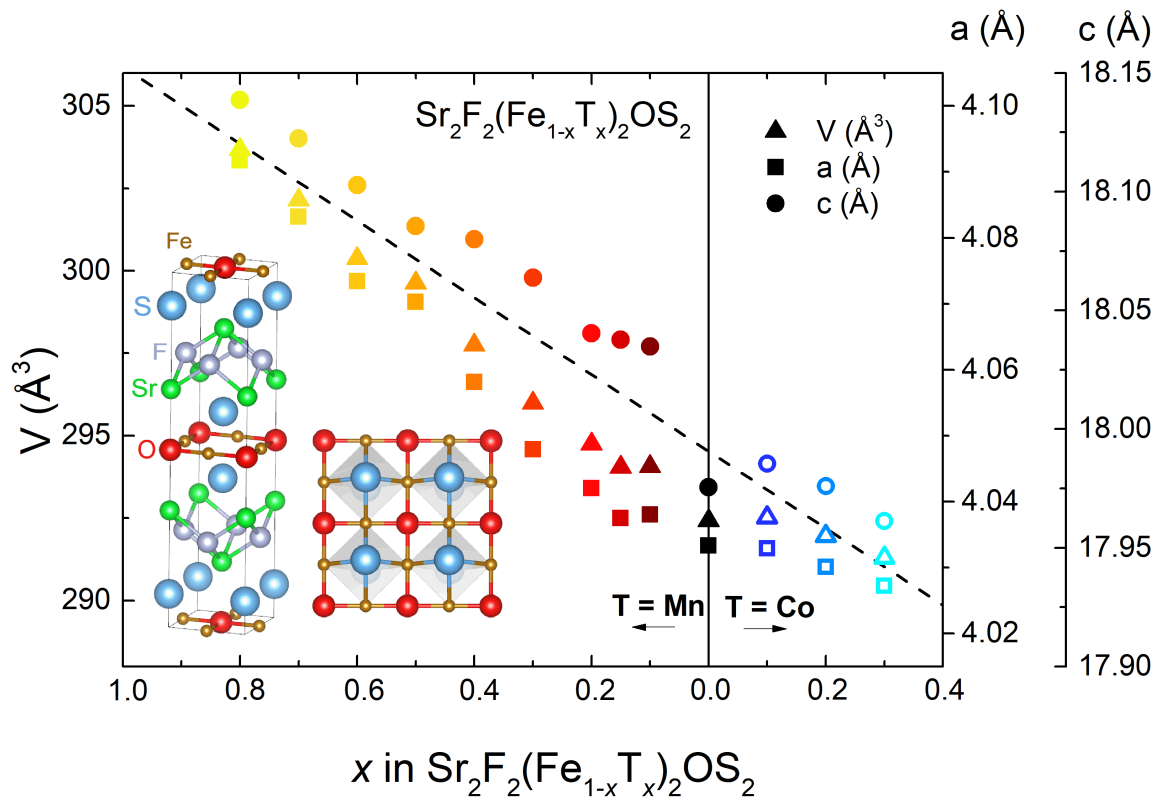


FIG. 1: Lattice parameters a (squares) and c (circles), and unit cell volume V (triangles) as a function of the Mn/Co content x in $\text{Sr}_2\text{F}_2(\text{Fe}_{1-x}\text{T}_x)_2\text{OS}_2$ ($T = \text{Mn}, \text{Co}$), the dashed line is a guide for the eye, highlighting the near-linear decrease of V throughout the composition range.

plane wave (FP-LAPW) method as implemented in the ELK package⁷ was used along with the generalized gradient approximation (GGA)⁸ for the exchange-correlation potential. The results were cross-checked using the WIEN2K package⁹, yielding similar results. The effects of Hubbard U on the band structure in the magnetically ordered phases were captured within the DFT+ U method¹⁰.

Neutron diffraction data were acquired on the time-of-flight POWGEN powder diffractometer at the Spallation Neutron Source (SNS) at Oak Ridge National Laboratory at temperatures between 12 K and 300 K on the parent compound and a Mn-doped sample with $x = 0.5$. Data was taken using two different instrumental configurations with neutron wavelength bands of 1.066 – 2.132 Å and 4.264 – 5.330 Å respectively for crystal and magnetic structure determination. FULLPROF¹¹ was used to perform Rietveld refinement on neutron diffraction data taken at $T = 300$ K.

III. RESULTS

A. Crystal Structure

Fig. 1 shows the crystal structure of the parent compound, $\text{Sr}_2\text{F}_2\text{Fe}_2\text{OS}_2$, and a graph of the lattice parameters and unit cell volume of the synthesized $\text{Sr}_2\text{F}_2(\text{Fe}_{1-x}\text{T}_x)_2\text{OS}_2$ ($T = \text{Mn}, \text{Co}$) series as determined from Rietveld refinements of X-ray diffraction data. The lattice parameters a , c , and unit cell volume V vary linearly with dopant content x , as expected from Vegard's law. The systematic variation of unit cell dimensions in substituted compounds is directly associated with the different ionic radii of the transition metal dopants¹² ($R_{\text{Mn}^{2+}} > R_{\text{Fe}^{2+}} > R_{\text{Co}^{2+}}$); consequently, Mn and Co substitution can be viewed as negative and positive chemical pressures, respectively.

Refinement of the crystal structure from neutron diffraction data is also in close agreement with the X-ray refinement, with lattice parameters $a = 4.0362(5)$ Å and $c = 17.9915(1)$ Å for the parent compound, which increase slightly to $a = 4.0706(4)$ Å and $c = 18.0930(3)$ Å for the Mn-substituted compound with $x = 0.50$. We looked closely at the details of the neutron diffraction refinement, to determine whether Fe and Mn are ordered or random upon in $\text{Sr}_2\text{F}_2\text{FeMnOS}_2$. Based on residual

values $\chi^2 = 18.7$ and 89.3 for the random and ordered moment configuration, we conclude that Fe and Mn randomly distribute on the transition metal site.

B. Magnetic Susceptibility

The magnetic properties of $\text{Sr}_2\text{F}_2(\text{Fe}_{1-x}\text{T}_x)_2\text{OS}_2$ are strongly dependent on the transition metal composition. As shown in the lefthand panel of Fig. 2, the temperature-dependent DC magnetic susceptibility, M/H , exhibits a systematic evolution as the dopant content varies. For the undoped ($x = 0$) compound, a well defined peak at $T_N = 110$ K (with a corresponding pronounced minimum in dM/dT [middle panel, Fig. 2]) marks the transition to 2D AFM order as established by magnetic neutron diffraction.⁷ Below T_N , irreversibility between the ZFC and FC data indicates magnetic frustration.⁷ Initially, Mn substitution shifts the AFM transition temperature to a minimum around 63 K for $x = 0.15$ in $\text{Sr}_2\text{F}_2(\text{Fe}_{1-x}\text{T}_x)_2\text{OS}_2$, with a less pronounced feature at T_N and significantly reduced irreversibility in the AFM ordered state for $x = 0.15$ compared to the parent compound.

As x increases above 0.15, the peak in $M(T)$ is further suppressed, evolving into a broad maximum at T_N , below which a bifurcation between the ZFC and FC curves shows up again at T_{irr} and becomes even more pronounced for compounds with higher x . Below T_{irr} , the ZFC magnetization drops with decreasing T while the FC curve turns slightly upward, which resembles the typical behavior of a frozen spin glass. AC susceptibility and heat capacity measurements substantiate a spin glass phase as will be discussed below. For $x \geq 0.3$, the feature at T_{irr} is flattened at the top and transforms into a plateau, while the minimum in dM/dT (middle panel, Fig. 2) persists. As shown later in the analysis of the neutron diffraction data, the minimum in the derivative is in fact associated with the development of 3D antiferromagnetic order. The critical temperature, taken as this local minimum in dM/dT , is denoted as T_N as we shall show it to be associated with collinear G-type Neel order. This is to be distinguished from the critical temperature T_{NV} of the parent compound, which is associated with a two- \mathbf{k} non-collinear 2D spin structure that we identify as a spin-vortex crystal. As x increases from 0.3 to 0.6, T_N increases monotonically, from 25 K ($x = 0.3$) to 90 K ($x = 0.7$).

In contrast to Mn substitution which suppresses the order of the parent compound $\text{Sr}_2\text{F}_2\text{Fe}_2\text{OS}_2$, Co substitution enhances T_{NV} , which reaches ≈ 127 K for $x = 0.3$. While cobalt substitution surely introduces disorder into the magnetic sublattice, which is generally detrimental to magnetic order, the Co-induced enhancement of the ordering temperature could result from the decrease in the lattice parameters, which reduces the average distance between magnetic ions and leads to stronger exchange interactions. There could

also be changes in the relative strengths of competing exchange interactions that favor the spin-vortex state. As for the Mn-substituted compounds with low x , the irreversibility in the AFM ordered state is reduced as the amount of Mn increases, which is likely an effect of the disorder lifting frustration-induced degeneracies.

While the spin glass-like features observed in the DC $M(T)$ data for a few intermediate compositions likely indicate a low-temperature spin glass state, it is necessary to perform AC susceptibility measurements to verify the most important hallmarks of spin glasses. As a sensitive probe of the relaxation process in the glassy state, the AC susceptibility of a spin glass system is expected to show a peak around the freezing temperature T_f , which moves towards higher temperatures with the frequency of the AC excitation field. Fig. 2 (right panel) shows the real part of the AC susceptibility, $\chi'(T)$, for selected compositions of $\text{Sr}_2\text{F}_2(\text{Fe}_{1-x}\text{T}_x)_2\text{OS}_2$ ($\text{T} = \text{Mn}, \text{Co}$). For $x = 0$, a double peak appears around $T_{NV} = 110$ K, which corresponds to the maximum and minimum in dM/dT (middle column, Fig. 2). In addition, the AC susceptibility exhibits a broad feature around $T_2 = 28$ K, that can also be traced in both the ZFC and FC DC $M(T)$ data (left panel, Fig. 2). Our neutron diffraction experiments reveal no additional magnetic Bragg peaks at $T = 12$ K other than those associated with AFM ordering at T_{NV} ,⁷ so the origin of the anomaly at T_2 remains unknown at this point. Possibilities to be explored include a subtle additional symmetry breaking or a cross-over in magnetic domain-wall dynamics of the 2D spin-vortex crystal.

Upon Mn doping in $\text{Sr}_2\text{F}_2(\text{Fe}_{1-x}\text{T}_x)_2\text{OS}_2$, a broad peak shows up in the AC data for $0.2 \leq x \leq 0.5$, shifting to lower temperatures as x increases. As the AC frequency increases, the peak position T_f increases monotonically, with $\Delta T_f/T_f \Delta(\ln \omega) \leq 0.8$ across all compositions, which is typical for a spin glass.⁷ For the same intermediate composition range, the freezing temperature T_f also coincides with T_{irr} , the temperature where ZFC and FC curves bifurcate as measured in DC $M(T)$ data (left panel, Fig. 2). At $x = 0.5$, while the AC susceptibility data retain a frequency-dependent feature at $T_f \approx 15$ K, it is no longer as symmetric and pronounced as for $x = 0.3$ and $x = 0.4$. In addition, AC data for $x = 0.5$ shows a much higher and narrower peak at $T_N = 42$ K, where the DC $M(T)$ data (Fig. 2) exhibit a step-like feature. T_N is independent of frequency, which indicates rapid relaxation. The magnetic properties of the $x = 0.5$ compound are reminiscent of reentrant spin glasses—a spin glass in which the material can enter a glassy state from either an AFM or FM ordered state during cooling as a consequence of competing exchange interactions. For $x > 0.5$, the AC susceptibility data also show a sharp peak at T_N and a broader feature at T_{irr} . However, no frequency dependence is observed, suggesting the absence of any collectively frozen state. Therefore, while the irreversibility in $M(T)$ data may be attributed to frustration and short range

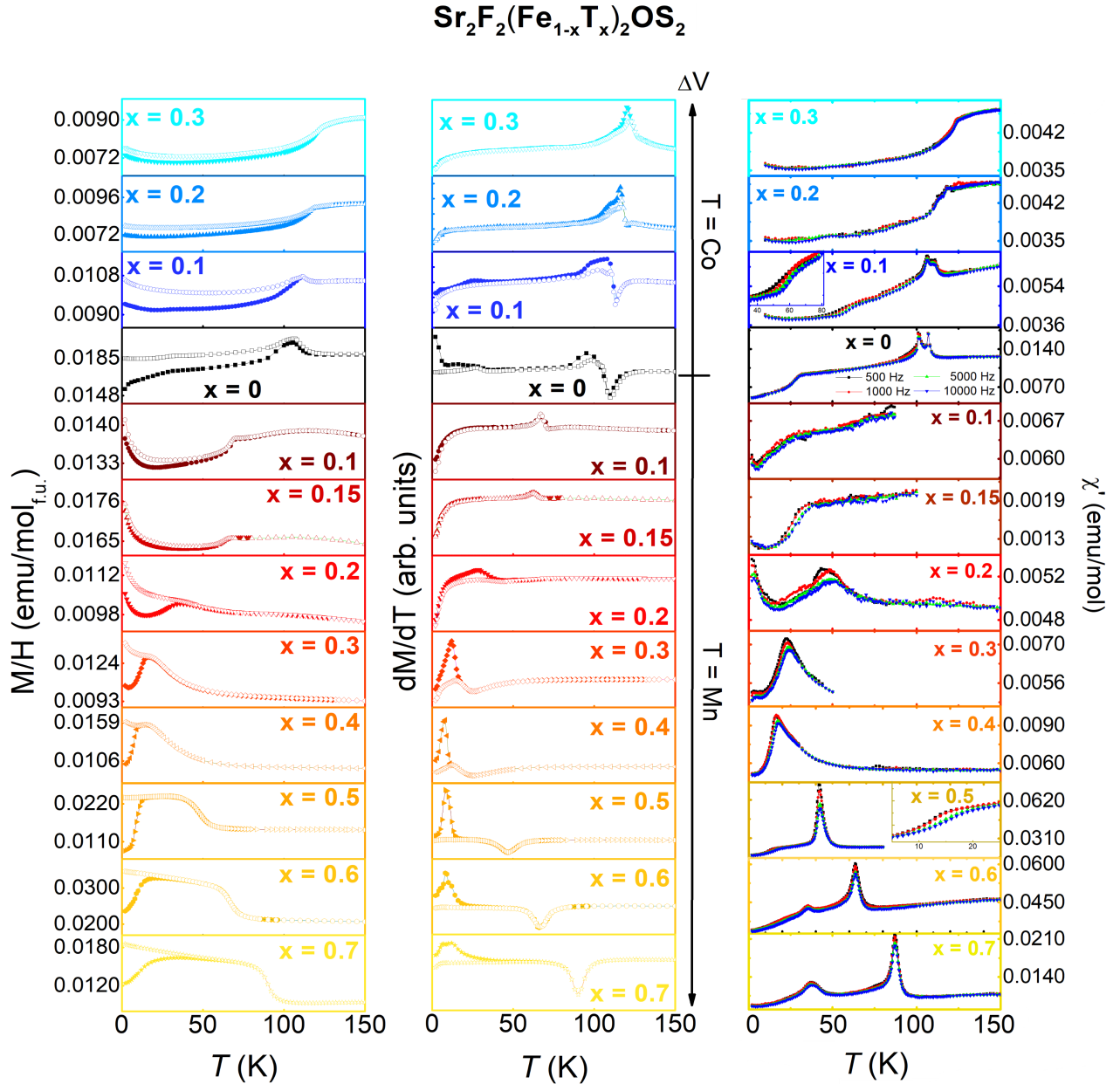


FIG. 2: $\text{Sr}_2\text{F}_2(\text{Fe}_{1-x}\text{T}_x)_2\text{OS}_2$ ($\text{T} = \text{Mn}, \text{Co}$) DC susceptibility M/H (left panels) and dM/dT (middle panels), together with AC susceptibility $\chi'(T)$ (right panels) for $f = 500, 1000, 5000,$ and 10000 Hz. The ZFC and FC data (left and middle) are marked with full and empty symbols, respectively.

correlations, $\text{Sr}_2\text{F}_2(\text{Fe}_{1-x}\text{Mn}_x)_2\text{OS}_2$ no longer exhibits spin glass behavior for $x \geq 0.5$.

For the Co-substituted compounds, the AC susceptibility data of $x = 0.1$ exhibits a double peak at T_N and a broad inflection at around 60 K, which resembles the pure compound at a first glance. However, unlike the pure compound, the broad feature at lower temperature that shows a dependence on the AC frequency. For the Co-substituted compounds with $x > 0.1$, no frequency dependence is observed. Nevertheless, it is possible that a spin glass state may

also exist in a narrow composition range close to $x = 0.1$

C. Resistivity

Arrhenius plots of the temperature-dependent resistivity for $\text{Sr}_2\text{F}_2(\text{Fe}_{1-x}\text{T}_x)_2\text{OS}_2$ ($\text{T} = \text{Mn}, \text{Co}$) compounds are shown in Fig. 3. Insulating behavior, as described by the Arrhenius law $\ln \rho = E_g/k_B T$, is observed for all compositions. The activation gap E_g , is determined from a linear fit of $\ln \rho$ vs. $1/T$. This

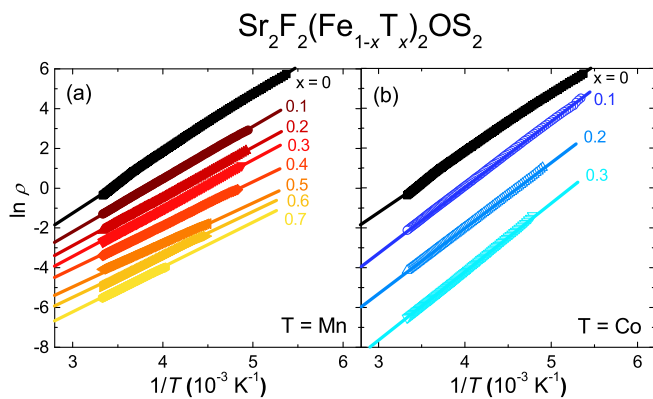


FIG. 3: Arrhenius plots for $\text{Sr}_2\text{F}_2(\text{Fe}_{1-x}\text{T}_x)_2\text{OS}_2$ for (a) $\text{T}=\text{Mn}$ ($x = 0, 0.1, 0.2, 0.3, 0.4, 0.5, 0.6, 0.7$) and (b) $\text{T}=\text{Co}$ ($x = 0, 0.1, 0.2, 0.3$). The data have been offset vertically for a clearer view. Linear fits to the Arrhenius law $\ln \rho = E_g/k_B T$ are shown in each graph.

data shown in Fig. 14 as part of concluding discussion. For the Mn-substituted compounds, E_g decreases nearly linearly as x increases from 0 to 0.5, indicative of more metallic behavior as a result of substitution. However, the gap starts to increase again as x increases above 0.5, creating a local minimum at or near $E_g(x = 0.5) = 0.18$ eV. For the Co-substituted compounds, the gap becomes larger as x increases, as a continuation of the linear trend seen in the Mn-substituted compounds with $0 \leq x \leq 0.5$. Considering the analogous linear dependence of unit cell volume on x (Fig. 1a) for both Mn- and Co-substituted compounds, it appears the systematic variation in E_g originates from the effect of chemical pressure on both the crystal and electronic structures of those materials. The deviation from the trendline, as observed in Mn-substituted samples with $x > 0.5$, suggests that other competing factors (e.g. electron counts) may also be at play, which yields the minimum in the gap energy at $x = 0.5$. While Mn-substitution alone is insufficient to drive this insulating compound into a metallic regime, it is still worth investigating whether additional tuning parameters, such as hydrostatic pressure or other dopings, can be applied on the $x = 0.5$ compound to drive it closer to the Mott transition. This study is currently underway.

D. Specific Heat

Heat capacity data for the Co- and Mn-substituted compounds are plotted in Fig. 4 and Fig. 5(a), respectively, scaled per mole of formula unit. For the undoped sample (black squares), the heat capacity exhibits a sharp peak at 107 K, which corresponds to the 2D Ising transition at T_{NV} . As Co is substituted for Fe, the peak gradually moves up with increasing x , consistent with the magnetization data (Fig. 2). For the Mn substituted samples, the peak vanishes for almost

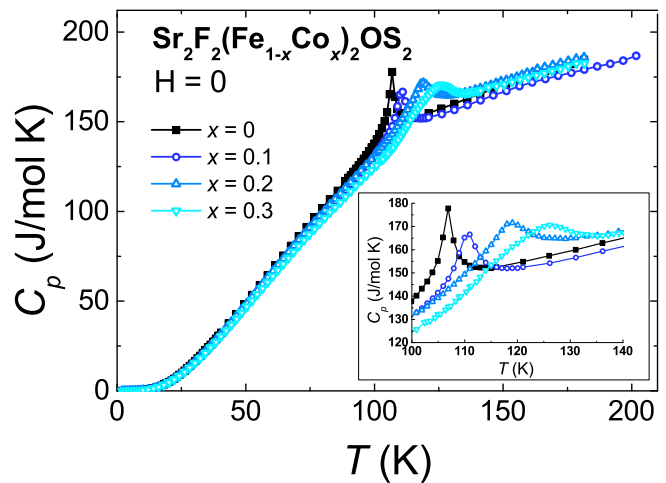


FIG. 4: Temperature-dependent heat capacity for $\text{Sr}_2\text{F}_2(\text{Fe}_{1-x}\text{Co}_x)_2\text{OS}_2$ ($x = 0, 0.1, 0.2, 0.3$).

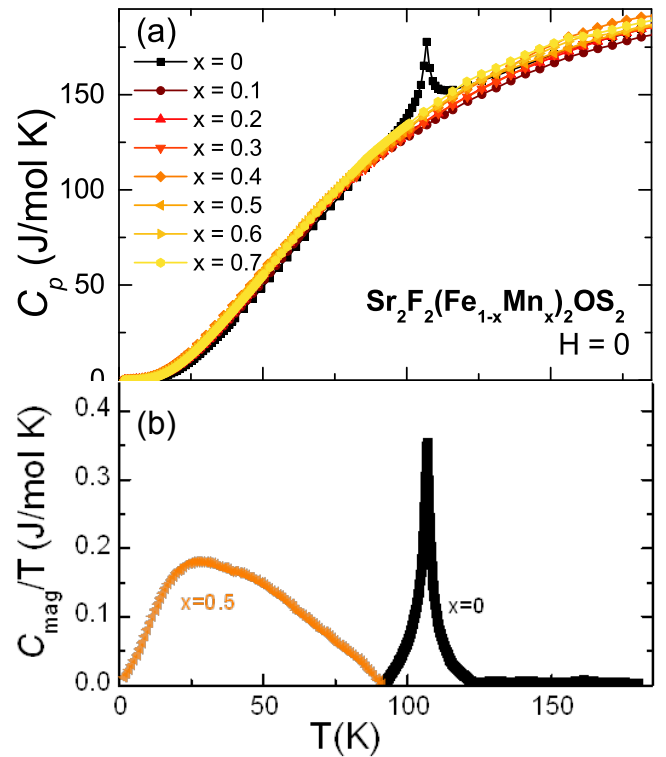


FIG. 5: (a) Temperature-dependent heat capacity C_p for $\text{Sr}_2\text{F}_2(\text{Fe}_{1-x}\text{Mn}_x)_2\text{OS}_2$ ($x = 0, 0.1, 0.2, 0.3, 0.4, 0.5, 0.6, 0.7$). (b) Magnetic heat capacity scaled by temperature C_{mag}/T for $x = 0$ (black) and $x = 0.5$ (orange), calculated as $C_{\text{mag}} = |C_p(x = 0) - C_p(x = 0.5)|$ (see text).

all compositions. No peak is anticipated in the spin glass-like regime. However, the absence of a peak for $x = 0.5$, where well defined anomalies are observed in dM/dT and $\chi'(T)$ (fig. 2) is a surprise. We shall also later see that magnetic neutron diffraction associated with G-type AFM order is detected for $T < 50$ K.

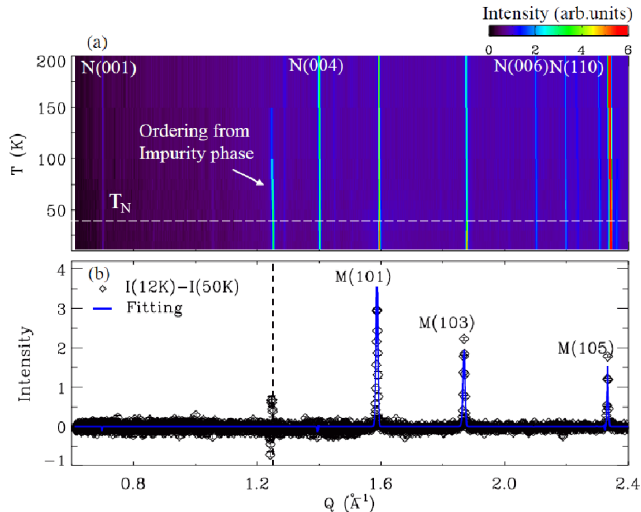


FIG. 6: $\text{Sr}_2\text{F}_2\text{FeMnOS}_2$. (a) Temperature dependence of neutron diffraction intensities from 300 K to 12 K. The horizontal dashed line marks T_N transition temperature. (b) The difference diffraction (square dots) and calculated (blue line) patterns between 12 K and 50 K ($T > T_N$). ‘M’ or ‘N’ represent the magnetic or nuclear Bragg peaks respectively. The vertical dashed line displays the wave vector position associated with ordering of the MnO impurity phase.

Fig. 5(b) shows the magnetic heat capacity scaled by temperature C_{mag}/T for $x = 0$ (black) and $x = 0.5$ (orange). Given the similarities in size and mass of Fe and Mn, it can be expected that their heat capacity curves only differ around the magnetic transitions, which are well separated for the two compositions shown in Fig. 5(b) ($T_{N,x=0} = 107$ K and $T_{N,x=0.5} = 45$ K). In the absence of a non-magnetic analogue, the magnetic heat capacity contribution can be estimated from the difference $C_{\text{mag}} = \Delta C_p = |C_{p,x=0} - C_{p,x=0.5}|$. The scaled C_{mag}/T in Fig. 5b indicates that Mn doping overall adds magnetic entropy to the system for a larger temperature range around T_N than in pure $\text{Sr}_2\text{F}_2\text{Fe}_2\text{OS}_2$. One possible explanation is that the G-type AFM order for $x = 0.5$ occurs only in a reduced volume fraction of the sample, where Mn and Fe ions are neighbors. We shall return to this point in the discussion of magnetic diffraction data.

E. Neutron Diffraction

Neutron diffraction experiments were conducted on the Mn-substituted compound $\text{Sr}_2\text{F}_2\text{FeMnOS}_2$. Fig. 6 shows the neutron diffraction intensity as a function of temperature and wavevector transfer Q . The Bragg peak at $Q \approx 1.25 \text{ \AA}^{-1}$ that develops upon cooling below $T = 116$ K cannot be indexed in the $\text{Sr}_2\text{F}_2\text{FeMnOS}_2$ unit cell and the critical temperature does not correspond to any bulk thermodynamic anomalies. It is attributed

IR	BV	Atom1 $m_x m_y m_z$	Atom2 $m_x m_y m_z$
Γ_3	$\psi(1)$	0 0 1	0 0 1
Γ_7	$\psi(2)$	0 0 1	0 0 -1
Γ_9	$\psi(3)$	1 0 0	0 0 0
	$\psi(4)$	0 0 0	-1 0 0
	$\psi(5)$	0 0 0	0 -1 0
	$\psi(6)$	0 1 0	0 0 0

TABLE I: $\text{Sr}_2\text{F}_2\text{FeMnOS}_2$. The 6 basis vectors associated with magnetic structures that transform according to irreducible representations with propagation vector $\mathbf{k} = (0, 0, 0)^?$.

to the magnetic ordering of a MnO impurity phase at the 10% volume fraction level. Looking more carefully for $T \approx T_N$, a temperature-dependent enhancement of Bragg scattering is observed at wavevector transfers $Q = 1.595 \text{ \AA}^{-1}$ and $Q = 1.877 \text{ \AA}^{-1}$, which correspond to the allowed nuclear Bragg peaks (101) and (103) respectively. This indicates the thermal anomalies observed in specific heat and susceptibility data at $T_N = 45$ K are associated with development of magnetic ordering with wavevector $\mathbf{k} = (0, 0, 0)$. Magnetic ordering along this vector is associated with an antiferromagnetic ground state. The lack of low-temperature enhancement in diffraction intensity for wavevectors $Q = n \times c$ that correspond Bragg peaks with $\mathbf{Q} \parallel \mathbf{c}$ such as $\mathbf{Q} = (0, 0, 2)$ and $\mathbf{Q} = (0, 0, 4)$ (Fig. 6) indicates the staggered magnetization is oriented along the \mathbf{c} -axis.

Using representation analysis implemented in SARAH[?], for $I4/mmm$ symmetry with a propagation vector $\mathbf{k} = (0, 0, 0)$, we find the reducible magnetic representation Γ_{mag} decomposes into four irreducible representations: $\Gamma_{\text{mag}} = \Gamma_3 + \Gamma_7 + 2\Gamma_9$ with a total of 6 basis vectors listed in Table I. Of these only Γ_7 describes an antiferromagnet with moments along \mathbf{c} . Fig. 6(b) shows the full magnetic diffraction pattern obtained by subtracting $T = 50$ K data from $T = 12$ K data is consistent with this structure.

In the corresponding G-type AFM spin configuration, which is also found in $\text{La}_2\text{O}_3\text{Mn}_2\text{Se}_2$ [?], the two spins in the asymmetric basis are antiparallel and oriented along $\hat{\mathbf{c}}$ (Fig. 7(b)). The remarkable change relative to the parent compound[?] indicates Mn-doping affects the competition between nearest and next nearest neighbor interactions within the basal plane that stabilizes the spin vortex crystal. The G-type antiferromagnet is favored by nearest neighbor antiferromagnetic interactions and next nearest neighbor ferromagnetic interactions so that Mn doping must shift those interactions correspondingly.

The ordered moment per formula unit inferred from the Rietveld analysis for $\text{Sr}_2\text{F}_2\text{FeMnOS}_2$ is $\langle M \rangle = 1.0(1)\mu_B$. This is significantly less than the ordered moment of the parent compound $(3.3(1)\mu_B)$.[?] Increased itineracy associated with the smaller activation gap and proximity to the Mott transition could be a factor here. However, it is also important to bear in mind that this is a 50% disordered alloy where each spin pair comes in four

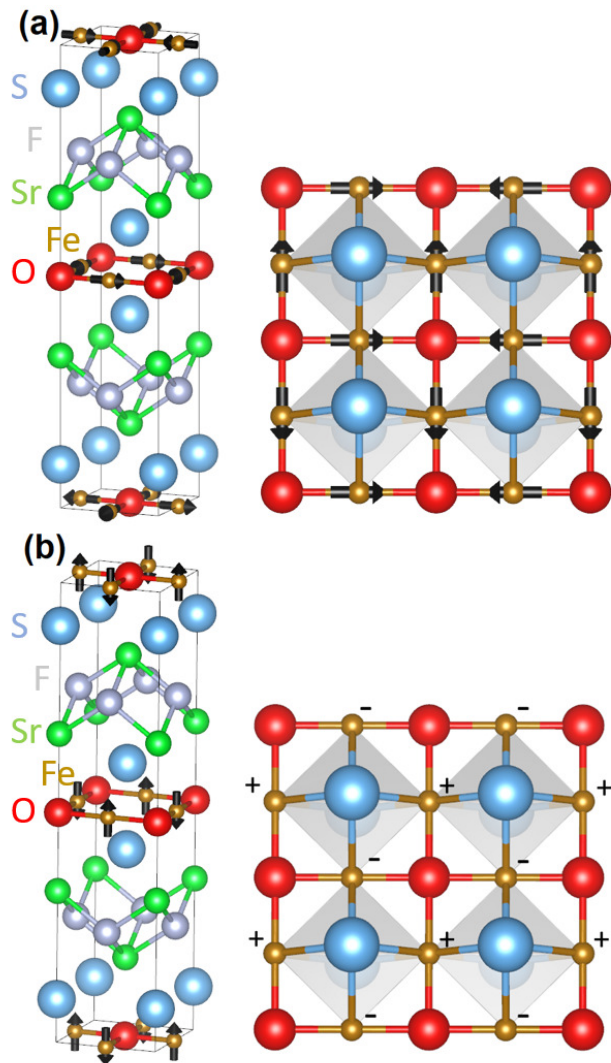


FIG. 7: $\text{Sr}_2\text{F}_2\text{Fe}_2\text{OS}_2$. (a) the unit cell with arrows indicating the Fe spins orientation in the AFM state, and the ab plane view of the Fe_2OS_2 . $\text{Sr}_2\text{F}_2\text{FeMnOS}_2$. (b) the unit cell with arrows indicating the Fe(Mn) spins orientation in the AFM state, and the ab plane view of the FeMnOS_2 layer with ‘+’ and ‘-’ symbols that denote the Fe(Mn) spins pointing up and down along c , respectively

variants Fe-Fe, Mn-Mn, Mn-Fe, and Fe-Mn perhaps with equal probability and magnetic Bragg scattering is only sensitive to the coherent component of magnetic order. If the effective ordered volume fraction is $0 < f < 1$ then our diffraction data implies the staggered moment within that volume fraction is given by $M_s = \langle M \rangle / \sqrt{f}$. Fig. 8(a-b) shows the Q -dependence of the magnetic component of the (101) and (103) diffraction peaks. Both peaks are resolution limited (horizontal bar), which indicates the magnetic correlation length exceeds 182 \AA . Rietveld refinement of the chemical structure indicates the Fe-Mn distribution is random on that length scale. The lack of a specific heat anomaly for $x = 0.5$ (Fig. 5)

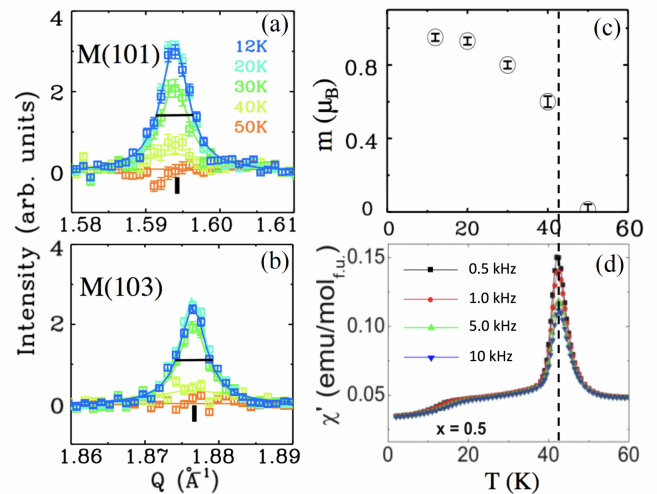


FIG. 8: (a-b) Magnetic peaks with wavevector at $Q = 1.595 \text{ \AA}^{-1}$ and $Q = 1.877 \text{ \AA}^{-1}$ associated with index M(101) and M(103) respectively. Data collected at $T = 60 \text{ K}$ were subtracted as a background. The solid lines are resolution convoluted Lorentzian fits. The horizontal bar indicates the instrumental resolution. The inferred correlation length from those fits is above 182 \AA . The vertical bars denote the peak positions. (c) The temperature dependence of the corresponding moment size per Fe(Mn). (d) AC magnetic susceptibility for $x = 0.5$, with the vertical dashed line indicating the coincidence of the magnetic order from these and the order parameter data in (c).

means we cannot exclude the possibility that full moment magnetic order occurs in a reduced volume fraction $f \geq (\langle M \rangle / M_s)^2 = (1.0 \mu_B / 3.3 \mu_B)^2 = 9\%$.

The temperature dependence of the staggered magnetization derived through Rietveld refinement of the neutron diffraction data is shown in Fig. 8(c). The relatively sharp onset of G-type AFM order is consistent with the sharp anomalies in magnetization data but at odds with the lack of a specific heat anomaly (Fig. 5). This suggests that the magnetic ordering involves a reduced volume fraction. The G-type AFM is unfrustrated which means that one possibility is a coherent magnetic order, with amplitude which varies through the sample in accordance with the particular local arrangements of Mn/Fe.

F. Electronic and Magnetic properties from *ab initio* calculations

To elucidate the electronic and magnetic properties of $\text{Sr}_2\text{F}_2\text{Fe}_2\text{OS}_2$ and $\text{Sr}_2\text{F}_2\text{FeMnOS}_2$, electronic structure calculations were performed using the density functional theory techniques described in section II. The density of states (DOS) in the paramagnetic phase exhibits narrow $3d$ bands of Fe and Mn around the Fermi level. With bandwidths of approximately 3.5 eV , they are narrower than the $3d$ bands in chalcogenides such

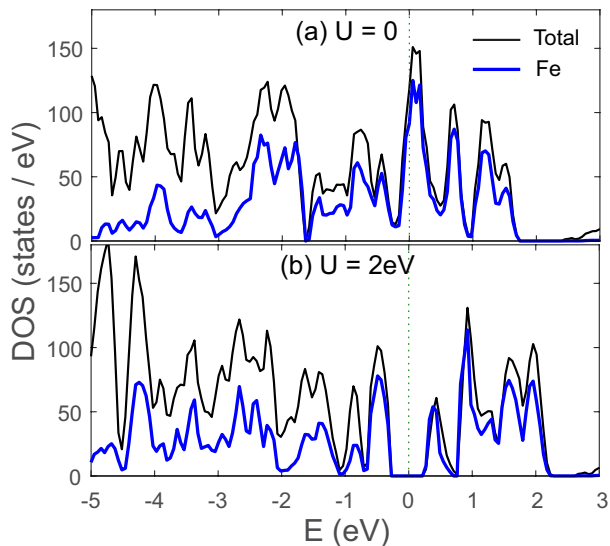


FIG. 9: Density of states for the two- \mathbf{k} magnetically ordered phase in $\text{Sr}_2\text{F}_2\text{Fe}_2\text{OS}_2$ from DFT and DFT+ U calculations. Partial contributions from electrons on Fe sites is shown in blue.

as LaOFeAs (~ 5.0 eV)[?] and BaFe_2As_2 , (~ 7.0 eV)[?]. This suggests enhanced electron correlations and localization, as reflected in the relatively high Néel temperatures, large magnetic moments and insulating behavior of these compounds. Therefore, the “22212”s are presumably closer to the parent compounds of cuprate superconductors at the strongly correlated end of the U/t chart.

Spin-polarized calculations were carried out on $\text{Sr}_2\text{F}_2\text{Fe}_2\text{OS}_2$ in the previously reported non-collinear two- \mathbf{k} spin structure[?] shown in Fig. 7(a). The DOS is plotted in Fig. 9, with the partial contribution from Fe sites also shown. In the absence of Hubbard interactions (top panel), the DOS shows a peak near the Fermi level arising from the minority spin channel in the Fe-3d orbitals, mainly comprised of the orbital corresponding to $m_l = 0$. A weak hybridization between 3d electrons of Fe and 2p/3p electrons of the chalcogens is consistent with fact that two of the 3d orbitals extend toward the oxygen and sulfur atoms. In $\text{Sr}_2\text{F}_2\text{Fe}_2\text{OS}_2$, the Fe ion is in a high-spin state has a moment of $3.2\mu_B$, close to the previously measured and calculated ordered moment[?].

In light of the above discussion on the role of strong electron correlations, the effects of Hubbard U on the band structure were captured within the DFT+ U method[?] inside the antiferromagnetic phase. The corresponding DOS (Fig. 9(b)) shows $U = 2.0$ eV is sufficient to open up a Mott gap at the Fermi level. The magnitude of U on Fe site is likely larger than 2 eV, however its specific value is immaterial, since we know that experimentally, the material is insulating and the present calculations serve as a proof of principle that the spectral Mott gap can be opened with a modest value of the Hubbard U .

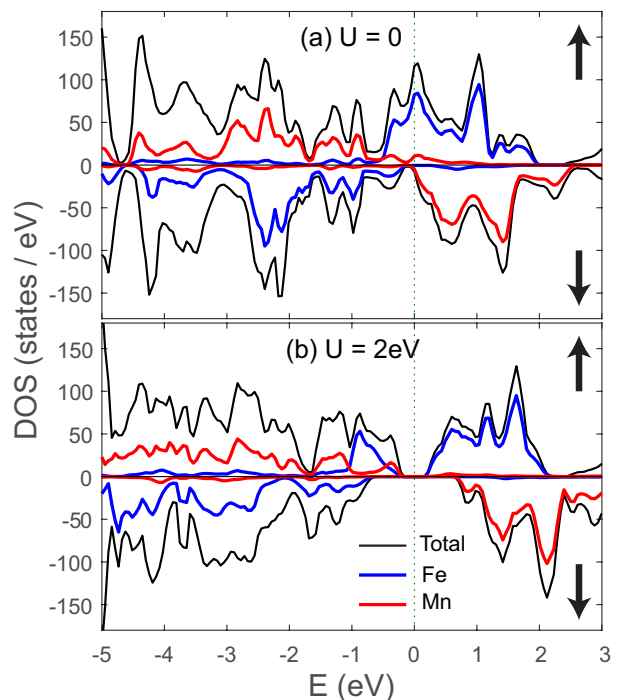


FIG. 10: Spin-polarized density of states in the G-type AFM ordered $\text{Sr}_2\text{F}_2\text{FeMnOS}_2$ from DFT and DFT+ U calculations. The top (bottom) sub-panels represent the majority (minority) spin-polarized DOS. The partial contributions from the Fe and Mn sites are shown in blue and red, respectively.

In $\text{Sr}_2\text{F}_2\text{FeMnOS}_2$, neutron diffraction has large contrast between Fe and Mn and shows these are disordered on the transition metal site, with a 50% probability of it being occupied by Fe or Mn ion. Since the solid-state DFT calculations require an ordered structure with periodic boundary conditions, we have chosen a checker-board periodic arrangement of nearest-neighbor Fe/Mn atoms. We have assumed the G-type AFM order as the ground state, shown in Fig. 7(b), as determined from our neutron measurements (see Sec. III E). The spin-polarized DOS for majority (minority) spin is plotted in the upper (lower) sub-panels of Fig. 10, respectively. In the absence of Hubbard interactions (top panel), the DOS shows a peak near the Fermi level, which disappears at a modest value of Hubbard U of 2eV, opening up a Mott insulating gap (bottom panel), as for $\text{Sr}_2\text{F}_2\text{Fe}_2\text{OS}_2$.

The calculations indicate the magnetic moments on transition metal ions correspond to the high-spin configuration, consistent with the rather small crystal field splitting (about 0.4 eV between the lowest and highest orbitals), stemming from the short metal-ligand bond distances and weak $d-p$ hybridization. While the $3d^6$ -Fe ion develops a moment of $3.3\mu_B$, the half-filled $3d^5$ -Mn shell results in a higher moment of $4.1\mu_B$. As the spin-polarized DOS plots in Fig. 10 indicate, the magnetic moments of Fe and Mn ions are

antiparallel, resulting in an intra-unit cell ferrimagnetic moment of $1\mu_B$ according to the calculations. We stress however that this result is an artifact of us choosing an ordered Fe/Mn crystal structure (required for the DFT calculation), and that the structural disorder on the transition metal site impact both the uniform and staggered components of the spin order. The difference between the zero-field cooled and field-cooled magnetization data in Fig. 2 may indicate this incipient ferrimagnetism.

IV. DISCUSSION

A. Microscopic Spin Exchange Parameters

A question that naturally arises from our neutron diffraction measurements, is why the ordered spin structure of $\text{Sr}_2\text{F}_2\text{FeMnOS}_2$ (Fig. 7(b)) differs so dramatically from that of pure $\text{Sr}_2\text{F}_2\text{Fe}_2\text{OS}_2$ (Fig. 7(a)). While we observe true 3D G-type AFM order with a correlation length in excess of 182 Å in $\text{Sr}_2\text{F}_2(\text{Fe}_{1-x}\text{Mn}_x)_2\text{OS}_2$ ($x = 0.5$), the undoped compound displays quasi-2D spin-vortex ordering. There are four dominant exchange paths between transition metal (T) spins in T -O plane: 90° nearest-neighbor (n.n.) T -O- T interaction with coefficient J_O , a T -S- T n.n. superexchange via the out-of-plane sulfur dumbbell with coefficient J_S and a bond angle of 100.22° , a 180° next-nearest neighbor (n.n.n.) T -O- T superexchange interactions with coefficient J'_2 , and a n.n.n. T -S- T superexchange with coefficient J_2 . Based on the Goodenough–Kanamori rules in the high-spin Fe and Mn configurations, the n.n. interactions J_S and J_O between $d_{x^2-y^2}$ orbitals of transition metal must include a ferromagnetic contribution since they involve two orthogonal S and O p -orbitals in the intermediate state. This is however not the only contribution, since the direct hybridization between n.n. d_{xz} and d_{yz} orbitals results in an antiferromagnetic interaction J_d . In total, the n.n. interaction is the sum of these three contributions:

$$J_1 = J_O + J_S + J_d \quad (1)$$

and one expects it to be antiferromagnetic (similar to the iron pnictides⁷), as suggested by the previous band structure calculations on $\text{Sr}_2\text{F}_2\text{Fe}_2\text{OS}_2$ ⁷.

Similarly, one expects the n.n.n. interaction J'_2 across the 180° -angle T -O- T ($T=\text{Fe},\text{Mn}$) bond to be antiferromagnetic, since it involves two electrons in the intermediate singlet state in the same p -orbital on O atom. Indeed, we find antiferromagnetic $J'_2 \sim 20$ meV from our electronic structure calculations. By contrast, the superexchange interaction J_2 across the sulfur dumbbell involves two T -S- T bonds with an obtuse angle, and the sign of the exchange constant J_2 is not immediately clear. Our *ab-initio* calculations suggest that $J_2(\text{Mn-Mn}) \approx 8$ meV is

antiferromagnetic in the pure Mn compound, whereas the sign is negative (ferromagnetic) in $\text{Sr}_2\text{F}_2\text{Fe}_2\text{OS}_2$, with $J_2(\text{Fe-Fe}) \approx -7$ meV. In both cases, the average value of $J_{\text{nnn}} = (J_2 + J'_2)/2$ remains positive.

B. G-type antiferromagnet

The above analysis is insufficient by itself to determine the spin ordering type. Rather, what matters is the value of J_{nnn} compared to the n.n. interaction J_1 . The G-type Néel structure observed in $\text{Sr}_2\text{F}_2\text{FeMnOS}_2$ is obtained if J_1 is sufficiently large (classically, one requires $J_1 > 2J_{\text{nnn}}$ for the Néel phase to be stable). One plausible explanation for the dramatic effects of Mn substitution in $\text{Sr}_2\text{F}_2\text{FeMnOS}_2$ is that $J_1(\text{Mn-Mn})$ and $J_1(\text{Fe-Mn})$ are larger than $J_1(\text{Fe-Fe})$ in the pure $\text{Sr}_2\text{F}_2\text{Fe}_2\text{OS}_2$ compound. This hypothesis is supported by our *ab initio* calculations on the hypothetical pure Mn-compound $\text{Sr}_2\text{F}_2\text{Mn}_2\text{OS}_2$ (experimentally, x as high as 0.7 in $\text{Sr}_2\text{F}_2(\text{Fe}_{1-x}\text{Mn}_x)_2\text{OS}_2$ was synthesized), in which we find $J_1(\text{Mn-Mn}) \sim 40$ meV to be substantially enhanced compared to $J_1(\text{Fe-Fe}) \sim 15$ meV between Fe spins in $\text{Sr}_2\text{F}_2\text{Fe}_2\text{OS}_2$. From this, we can estimate that in $\text{Sr}_2\text{F}_2\text{FeMnOS}_2$ (at $x = 0.5$ Mn doping), because of the structural disorder on the transition metal site, the effective nearest-neighbor exchange coupling is an average over Fe-Fe, Fe-Mn, and Mn-Mn interactions as follows: $J_1^{\text{eff}} = [J_1(\text{Fe-Fe}) + J_1(\text{Mn-Mn}) + 2J_1(\text{Fe-Mn})]/4$. Since $J_1(\text{Mn-Mn})$ is much higher than $J_1(\text{Fe-Fe})$, as stated above, this leads to an enhanced value of J_1^{eff} , thus favoring a G-type AFM structure in $\text{Sr}_2\text{F}_2\text{FeMnOS}_2$.

C. Spin Vortex Crystal

The non-collinear two- \mathbf{k} spin ground state in $\text{Sr}_2\text{F}_2\text{Fe}_2\text{OS}_2$ deserves special attention that also leads to an understanding of the 2D Ising character of the magnetic phase transition in $\text{Sr}_2\text{F}_2(\text{Fe}_{1-x}\text{Mn}_x)_2\text{OS}_2$. The ordered spin structure in $\text{Sr}_2\text{F}_2\text{Fe}_2\text{OS}_2$ can be described rather elegantly as a checkerboard lattice of vortices and antivortices localized on oxygen atoms which are situated at the centers of the 4 Fe plaquettes (Fig. 11a). Mathematically, the planar spin texture $\vec{S} = (S_x, S_y)$ at position $\mathbf{r} = (r \cos \phi, r \sin \phi)$ around a vortex/antivortex can be written as follows:

$$S_y(\mathbf{r})/S_x(\mathbf{r}) = \tan(m \cdot \phi + \gamma), \quad (2)$$

where m is called “vorticity” and can be formulated in terms of the monopole charge⁷ of the corresponding vortex ($m = 1$) or antivortex ($m = -1$), whereas the helicity γ determines an angle by which all spins are rotated. Different types of (anti)vortices are shown in Fig. 11(b), from which it becomes clear that the blue and red vortices have the same vorticity $m = 1$, and can be transformed into each by rotating all spins by

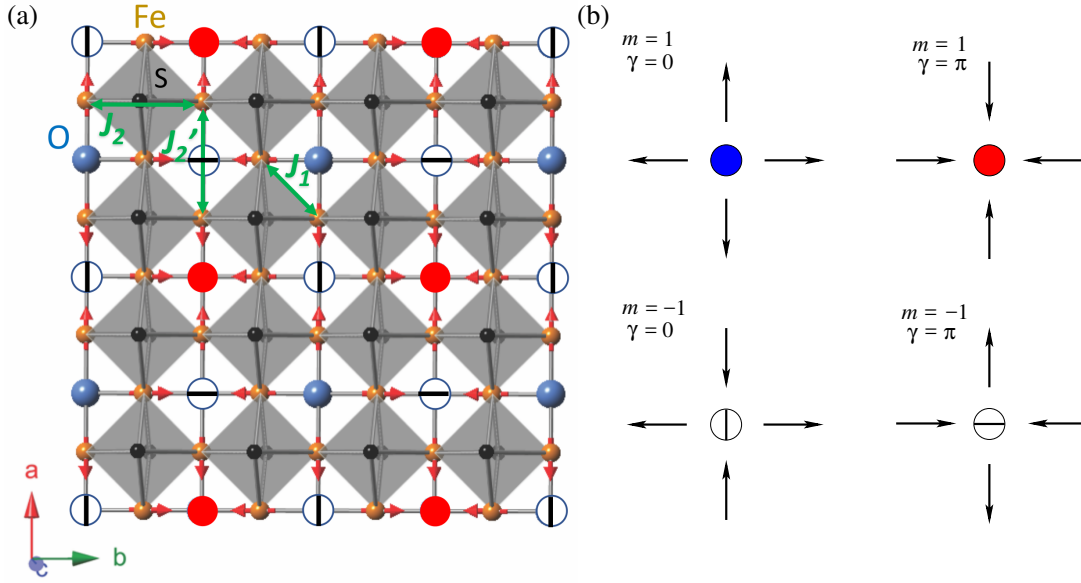


FIG. 11: (a) Experimentally determined spin structure in $\text{Sr}_2\text{F}_2\text{Fe}_2\text{OS}_2$ with the red, blue and white circles indicating oxygen atoms, which are identified as centers of either vortices or antivortices. Vortices (red and blue) have vorticity $m = 1$, whereas antivortices (white) have $m = -1$. (b) Schematic representation of the four type of (anti)vortices encountered in panel (a). In addition to vorticity, they are distinguished by the helicity γ defined in Eq. (2).

the angle $\gamma = \pi$. The same is true for the two types of antivortices denoted by white circles in the bottom row of Fig. 11(b). We conclude that the two- \mathbf{k} structure contains two kinds of vortices and antivortices, forming a rigid periodic lattice. We call this phase a *spin vortex crystal*, in accord with the nomenclature previously used in the literature^{???}. The spin vortices realized here are close cousins of skyrmions^{??}, although the latter are more complex non-coplanar objects with non-zero S_z spin component, compared to the in-plane spin structure of $\text{Sr}_2\text{F}_2\text{Fe}_2\text{OS}_2$. Nevertheless, both spin vortices and skyrmions are similar in that they are topological objects characterized by an integer invariant – vorticity or skyrmion number[?], respectively.

We note that the spin vortex crystal realized in $\text{Sr}_2\text{F}_2\text{Fe}_2\text{OS}_2$ bears some similarity to the one recently proposed in the context of the tetragonal magnetic phase of hole-doped iron pnictides^{??}, with the key difference that in the latter case, only vortices with $m = 1$ are present, arranged in a checkerboard pattern of blue/red circles with helicities $\gamma = 0$ and $\gamma = \pi$, respectively, as depicted in Fig. 12c. By contrast, $\text{Sr}_2\text{F}_2\text{Fe}_2\text{OS}_2$ harbors a total of four different vortex/antivortex types, as depicted in Fig. 11 and Fig. 12a. One can trace this difference to the reduced lattice symmetry of $\text{Sr}_2\text{F}_2\text{Fe}_2\text{OS}_2$, manifested in non-equal exchange couplings $J_2 \neq J_2'$ through the sulfur dumbbells and oxygen atoms, respectively. Moreover as already mentioned above, we find J_2 to be ferromagnetic in $\text{Sr}_2\text{F}_2\text{Fe}_2\text{OS}_2$, in stark contrast to the iron pnictides where J_2 is antiferromagnetic and isotropic along the C_4 -symmetric directions on the square lattice. This

explains why the vortex crystal proposed in Ref. ? is not observed here: it is energetically unfavorable because its in-plane \mathbf{Q} -vector $\mathbf{Q} = (1/2, 1/2)$ violates the ferromagnetic J_2 exchanges (dashed lines in Fig. 12c). The collinear spin stripe phase seen ubiquitously across multiple families of iron pnictides has the same \mathbf{Q} vector and is energetically disfavored for the same reason, as Fig. 12d illustrates. Instead, the two competing phases in $\text{Sr}_2\text{F}_2\text{Fe}_2\text{OS}_2$ have two \mathbf{Q} -vectors: they are the spin vortex crystal we observe (Fig. 12a) and a hypothetical collinear phase with the same biaxial two- \mathbf{Q} ordering (Fig. 12b). It is distinguished by the presence of the $\mathbf{Q} = (1/2, 0)$ Bragg peak in magnetic neutron scattering, which is not observed for $\text{Sr}_2\text{F}_2\text{Fe}_2\text{OS}_2$.

D. Effective Field Theory of the Magnetic State

One can get a better understanding of the origin of the non-collinear spin structure in $\text{Sr}_2\text{F}_2\text{Fe}_2\text{OS}_2$ by considering an effective field theory defined in terms of magnetic order parameters, \mathbf{M}_1 and \mathbf{M}_2 associated with the two ordering wave-vectors $\mathbf{Q}_1 = (1/2, 0, 1/2)$ and $\mathbf{Q}_2 = (0, 1/2, 1/2)$, respectively. However, unlike the simpler case of an isotropic square lattice considered in Ref. ? in the context of iron pnictides, the minimal description here requires treating two sublattices, A and B, depicted by the empty and full circles with arrows in Fig. 12:

$$\begin{aligned} \mathbf{M}(\mathbf{r}_A) &= \mathbf{M}_{1A}e^{i\mathbf{Q}_1 \cdot \mathbf{r}_A} + \mathbf{M}_{2A}e^{i\mathbf{Q}_2 \cdot \mathbf{r}_A} \\ \mathbf{M}(\mathbf{r}_B) &= \mathbf{M}_{1B}e^{i\mathbf{Q}_1 \cdot \mathbf{r}_B} + \mathbf{M}_{2B}e^{i\mathbf{Q}_2 \cdot \mathbf{r}_B}. \end{aligned} \quad (3)$$

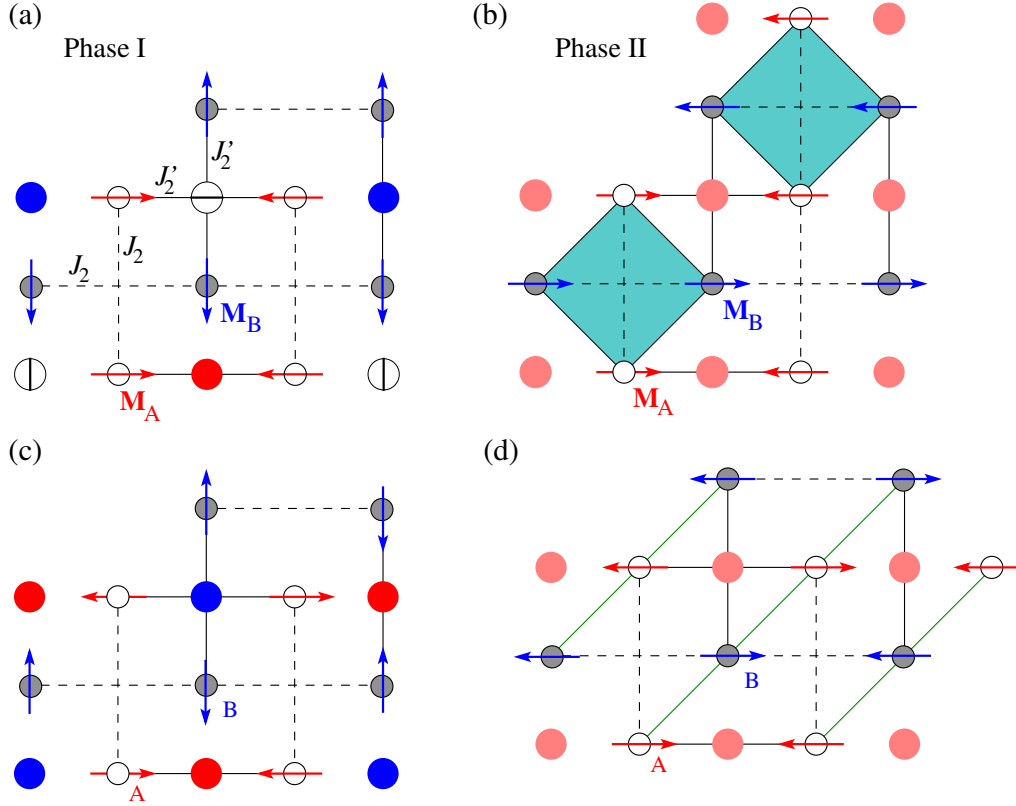


FIG. 12: Various phases that can be theoretically realized in a $J_1 - J_2 - J_2'$ model on a square lattice. The empty (filled) circles denote Fe sites on sublattice A (B) respectively. Note that J_2 exchanges (dashed lines) are ferromagnetic in $\text{Sr}_2\text{F}_2\text{Fe}_2\text{OS}_2$. The sulfur dumbbells where dashed lines meet were omitted for clarity. Pink circles depict oxygen atoms. (a) Spin-vortex crystal with $\mathbf{M}_A \perp \mathbf{M}_B$ as realized in $\text{Sr}_2\text{F}_2\text{Fe}_2\text{OS}_2$, with the blue/red/white circles denoting the centers of vortices/antivortices using the same notation as in Fig. 11. (b) Collinear structure with $\mathbf{M}_A \parallel \mathbf{M}_B$, which can be viewed as a staggered arrangement of 4-Fe plaquettes denoted by teal rhombi. (c) A different spin vortex crystal with $\mathbf{Q} = (1/2, 1/2)$ realized in $\text{La}_2\text{O}_2\text{Co}_2\text{OSe}_2$,[?] which was predicted in Ref. ?. Note that only two types of vortices (red and blue) appear, unlike in Phase I. (d) A collinear $\mathbf{Q} = (1/2, 1/2)$ structure resulting in a “spin stripe” phase common in the iron pnictides, with green lines denoting the direction of stripes.

The treatment can be somewhat simplified by noticing that at the free-field level, the lattice point-group symmetry imposes $|\mathbf{M}_{1A}| = |\mathbf{M}_{2B}|$, because the antiferromagnetic J_2' direction is horizontal (along \mathbf{Q}_1) for the A sublattice and vertical (along \mathbf{Q}_2) for the B sublattice, see Fig. 12. In other words, the quadratic part of the action is symmetric under the exchange of labels $A \leftrightarrow B$ and $1 \leftrightarrow 2$. This motivates us to lighten the notation with fewer subscripts and rewrite Eq. (3) as follows:

$$\begin{aligned} \mathbf{M}(\mathbf{r}_A) &= \mathbf{M}_A e^{i\mathbf{Q}_1 \cdot \mathbf{r}_A} + \mathbf{m}_A e^{i\mathbf{Q}_2 \cdot \mathbf{r}_A} \\ \mathbf{M}(\mathbf{r}_B) &= \mathbf{M}_B e^{i\mathbf{Q}_2 \cdot \mathbf{r}_B} + \mathbf{m}_B e^{i\mathbf{Q}_1 \cdot \mathbf{r}_B}, \end{aligned} \quad (4)$$

in terms of which the quadratic part of the action takes the form:

$$S_2 = \int_{\mathbf{q}} \chi_M(\mathbf{q})^{-1} (\mathbf{M}_A^2 + \mathbf{M}_B^2) + \int_{\mathbf{q}} \chi_m(\mathbf{q})^{-1} (\mathbf{m}_A^2 + \mathbf{m}_B^2). \quad (5)$$

The susceptibilities have the generic form $\chi_l(\mathbf{q})^{-1} = r_l(T) + c_l \mathbf{q}_l^2$ ($l = M, m$) in terms of

the in-plane wave-vector \mathbf{q}_{\parallel} expanded around the appropriate ordering vector, where we've ignored the q_z dependence for the sake of simplicity and because the phase transition we seek to describe in $\text{Sr}_2\text{F}_2\text{Fe}_2\text{OS}_2$ is to a 2D ordered state.

The key point is that the two susceptibilities are *not* equal, $\chi_m \neq \chi_M$ because the lattice lacks the C_4 rotational symmetry around the A (or B) site. In the case of M_A and M_B , those order parameters respect the ferromagnetic exchange $J_2 < 0$ across the sulfur dumbbell, and one expects to see an ordering at a finite temperature T_M , so that $r_M = a_M(T - T_M)$. By contrast, the orders m_A and m_B violate the exchange couplings (see Fig. 13) and are energetically disfavored, so that the corresponding quadratic coefficient is always positive, $r_m > 0$, resulting in $|\mathbf{m}_A| = |\mathbf{m}_B| = 0$. We conclude that one can safely remove these two components from consideration of the ground state properties and formulate the low-energy effective theory in terms of \mathbf{M}_A and \mathbf{M}_B alone. Based on the symmetry arguments, the most general quartic terms allowed by

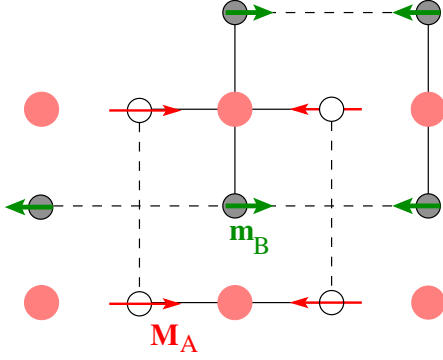


FIG. 13: A hypothetical structure with a single $Q_1 = (1/2, 0)$ order in plane, corresponding to non-zero M_A and m_B (and $M_B = 0$). Note that m_B order would violate both the FM J_2 couplings (dashed lines) and AFM J_2 couplings (solid lines). The most likely outcome is that $m_B = 0$ and only sublattice A is ordered, as would be the case if $g > \max(0, -w)$ in Eq. (6).

spin-rotational symmetry are the following three^{???} :

$$S_4[\mathbf{M}_A, \mathbf{M}_B] = u \int_x (\mathbf{M}_A^2 + \mathbf{M}_B^2)^2 - g \int_x (\mathbf{M}_A^2 - \mathbf{M}_B^2)^2 + 4w \int_x (\mathbf{M}_A \cdot \mathbf{M}_B)^2, \quad (6)$$

It is the quartic coefficients u , g and w that determine the nature of the magnetic ground state. One can derive them in principle from a microscopic $J_1 - J_2 - J_2'$ model, as was done for the isotropic $J_1 - J_2$ model using, for instance, the $1/S$ expansion[?], however we shall consider them as phenomenological parameters, which is appropriate in the spirit of an effective field theory. First if $g < \max(0, -w)$, the action is minimized by $|\mathbf{M}_A| = |\mathbf{M}_B|$, with either

$$\begin{cases} \mathbf{M}_A \perp \mathbf{M}_B & \text{for } w > 0: \quad \text{Phase I (Fig. 12a)} \\ \mathbf{M}_A \parallel \mathbf{M}_B & \text{for } w < 0: \quad \text{Phase II (Fig. 12b)} \end{cases}$$

Another possibility is if $g > \max(0, -w)$, in which case the optimal solution is found with $\mathbf{M}_A = 0$ or $\mathbf{M}_B = 0$. This corresponds to the absence of the ordered moment on one of the sublattices, spontaneously breaking the $A \leftrightarrow B$ symmetry of the crystal, and was dubbed “charge-spin density wave” in Ref. [?]. It is however not realized in any of the materials studied here.

We conclude that $g < 0$ while $w > 0$ in $\text{Sr}_2\text{F}_2\text{Fe}_2\text{OS}_2$, since we know from neutron diffraction[?] that Phase I spin-vortex crystal is realized in this compound (Fig. 12a). This state has a non-zero vector chirality $\langle \vec{\phi}_{ch} \rangle = \langle \mathbf{M}_A \times \mathbf{M}_B \rangle$, and can be thought of as having an emergent Dzyaloshinskii-Moriya (DM) interaction $\langle \vec{\phi}_{ch} \rangle \cdot (\mathbf{M}_A \times \mathbf{M}_B)$, dynamically generated by the magnetic frustrations. While the absence of inversion symmetry through the center of the nearest-neighbor A-B bond allow for the DM interaction of the form $\mathbf{D} \cdot \mathbf{S}_i \times \mathbf{S}_j$, the mirror plane implies $D_z = 0$ so there can be no impact on $\langle \vec{\phi}_{ch} \rangle$.

The discrete character of the vortex and helicity indices $m = \pm 1$, $\gamma = \{0, \pi\}$ imparts an emergent Ising character to the phase transition into the spin vortex phase. This is manifest in the Onsager form for the T -dependent order parameter in $\text{Sr}_2\text{F}_2\text{Fe}_2\text{OS}_2$ and the distinct 2D character of the ordered state. Our alloying studies support the notion that the 2D Ising character is of emergent nature rather than a result of a single-ion anisotropy since, when Mn doping enhances the NN AFM interaction, the resulting phase transition is fully three dimensional even though inter-plane interactions should not increase significantly.

The above effective field theory gives us another perspective on the emergent Ising nature of the transition: in the PM state, the order parameters \mathbf{M}_A and \mathbf{M}_B on the two sublattices are independent of each other, and assuming an easy-plane single-ion anisotropy typical of Fe in similar materials (e.g. iron pnictides), the total spin symmetry is $SO(2) \times SO(2)$ in the paramagnetic phase. Upon approaching the spin-vortex phase, Fig. 12a), the positive quartic term $w > 0$ dictates that the fluctuating moments satisfy $\mathbf{M}_B \perp \mathbf{M}_A$, reducing the symmetry down to $SO(2) \times \mathbb{Z}_2$ (for a given \mathbf{M}_A direction, \mathbf{M}_B can only point in one of the two perpendicular in-plane directions). Equivalently, one can see the emergent \mathbb{Z}_2 (Ising) symmetry as associated with the vector chirality $\phi_{ch} = \hat{z} \cdot (\mathbf{M}_A \times \mathbf{M}_B)$ which must point up or down along the \hat{z} direction. In the language of vortices in Fig. 11b), the Ising symmetry $\phi_{ch} \rightarrow -\phi_{ch}$ corresponds to flipping the direction of spins on, say, the B sublattice, which changes vorticity $m \rightarrow -m$ and transforms red/blue vortices into the corresponding antivortices.

In cases like this with $SO(2) \times \mathbb{Z}_2$ symmetry in quasi-2D systems, it is known^{??} that the Ising \mathbb{Z}_2 transition can take place first, followed closely by the Kosterlitz–Thouless transition at a slightly lower temperature into a phase with quasi-long-range spin order of XY spins. The present observation of the Ising nature of the transition points to the likely realization of this phenomenon in $\text{Sr}_2\text{F}_2\text{Fe}_2\text{OS}_2$, with the chirality order parameter ϕ_{ch} playing the role of the emergent Ising variable. Said differently, the Ising transition corresponds to the binary choice of seeding vortices/antivortices on the crystalline lattice, with one of the two configurations shown in Fig. 11.

We should add that the above effective field theory analysis was performed under the assumption that the magnetic moments are rotationally symmetric within the easy (ab) plane, and the phase transition into the vortex phase occurs via the spontaneous breaking of this symmetry. It is however possible that the rotational symmetry is approximate and is broken from the outset, as one might expect given the absence of local C_4 symmetry around the A and B sites. In this case, the effective field theory equations (5) and (6) still hold, with the caveat that single-ion anisotropy terms should be added to reflect the loss of the spin-rotational symmetry

at the bare field level. While this would serve to remove the continuous symmetry breaking, the key result of our analysis still stands: namely, the Ising variable $\phi_{ch} = \hat{z} \cdot (\mathbf{M}_A \times \mathbf{M}_B)$ can still develop a long-range order, thus resulting in the spin vortex crystal. Such a spontaneous breaking of a discrete (Ising) symmetry is immune to the Mermin-Wagner theorem and can therefore take place at a finite temperature in two spatial dimensions, explaining the apparent Ising nature of the transition observed experimentally.

In summary, both the simpler G-type Néel order in $\text{Sr}_2\text{F}_2\text{FeMnOS}_2$ and the two- \mathbf{k} non-collinear spin-vortex structure in $\text{Sr}_2\text{F}_2\text{Fe}_2\text{OS}_2$ can be understood in the framework of a local-moment microscopic $J_1 - J_2 - J'_2$ model and the effective field theory as described above. Note that the insulating nature of these materials and the high-spin configuration of the transition metal ions make the $J_1 - J_2 - J'_2$ theory of local moments ideally suited for their description, in contrast to the iron pnictides where the itinerant nature of the electrons requires consideration of the Fermi surface nesting instability and the associated magnetic orders^{????}. Among Mott insulating compounds, $\text{Sr}_2\text{F}_2\text{Fe}_2\text{OS}_2$ is, to the best of our knowledge, the only compound in which a spin vortex crystal is realized, following the theoretical predictions of them occurring in certain types of frustrated spin systems^{???}. The closest known analog is the hole-doped $\text{CaKFe}_4\text{As}_4$ [?], although the present structure is richer, with four different types of vortices/antivortices arranged in a periodic lattice as shown in Fig. 11.

V. CONCLUSIONS

Doping $\text{Sr}_2\text{F}_2\text{Fe}_2\text{OS}_2$ with Co and Mn have opposite effects with respect to magnetism and electrical transport: Co appears to stabilize the spin-vortex crystal of the parent compound as indicated by an increase in T_N . Mn, on the other hand, suppresses the AFM order in favor of a spin glass state as confirmed by AC susceptibility measurements. At 50% doping, Mn causes a transformation of the parent compound's quasi-2D non-collinear spin structure into a G-type AFM structure typical of other layered Mott insulators with the same structure such as $\text{La}_2\text{O}_3\text{Mn}_2\text{Se}_2$. Additionally, while Co doping increases the gap energy in a monotonic, linear fashion, Mn doping decreases the gap energy until a minimum is reached at $x=0.5$, followed by a subsequent increase for $0.5 < x \leq 0.7$ in $\text{Sr}_2\text{F}_2(\text{Fe}_{1-x}\text{Mn}_x)_2\text{OS}_2$. Fig. 14 summarizes the effects of Mn and Co doping on the energy gap and the features observed in specific heat, AC magnetization, and DC magnetization measurements.

The observed trends can be reasonably well explained if we consider the effects of Mn and Co doping in terms of disorder and chemical pressure. The positive chemical pressure exerted by Co, reflected in the volume change

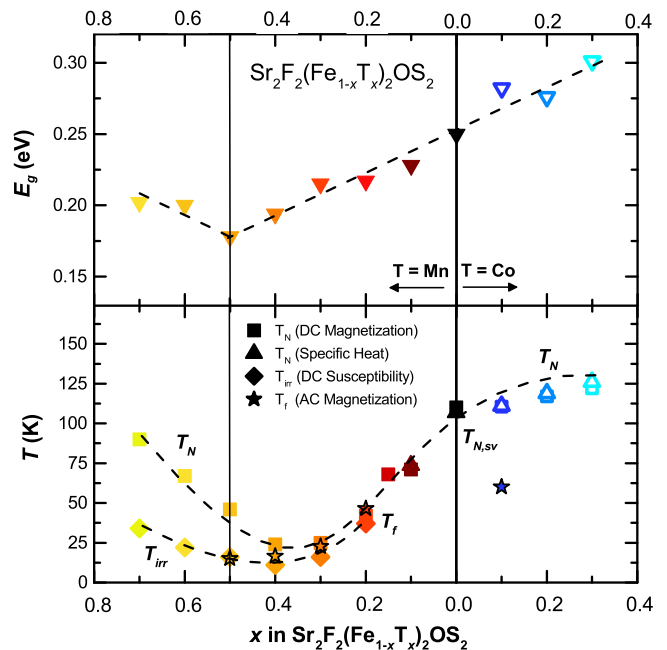


FIG. 14: A phase diagram showing energies determined from Arrhenius fits and ordering temperatures as determined from magnetization and specific heat measurements. T_f was determined from 500 Hz AC susceptibility data.

ΔV in Fig. 1, causes a reduction in the lattice parameters which enhances the magnetic exchange interactions. The effect is strong enough to increase T_C and stabilize the AFM order despite the inevitable disorder introduced by doping. Conversely, as Mn doping is analogous to a negative pressure, we expect the magnetic exchange interactions to be weakened as the unit cell volume increases.

Substituting Mn also has the effect of increasing the strength of the nearest-neighbor spin-spin interaction, as indicated by our *ab initio* electronic structure calculations and theoretical analysis. As a result, $\text{Sr}_2\text{F}_2\text{FeMnOS}_2$ (and presumably other $\text{Sr}_2\text{F}_2(\text{Fe}_{1-x}\text{Mn}_x)_2\text{OS}_2$ compounds for sufficiently large x) form a simple and fully three dimensional Néel magnetic ground state, in contrast to $\text{Sr}_2\text{F}_2\text{Fe}_2\text{OS}_2$, which forms a quasi-two-dimensional non-collinear two- \mathbf{k} spin structure. The latter is a *spin vortex crystal* predicted theoretically to exist in certain types of frustrated spin systems^{???}. We find that upon Mn substitution, the transition from this spin vortex crystal phase into conventional 3D Néel order occurs via an intermediate spin-glass phase, indicative of competition between these two states.

A number of questions remain, however, that require further study: Can the energy gap in the bandstructure of $\text{Sr}_2\text{F}_2\text{FeMnOS}_2$ be closed with pressure or doping? Will successful tuning of the localized Mott insulating state into an itinerant metallic state produce a high-temperature superconducting ground state and

provide new insight into the interplay between quantum magnetism and superconductivity? The minimum in gap energy and the reduced ordered moment found in $\text{Sr}_2\text{F}_2\text{FeMnOS}_2$ are promising indicators that we are close to achieving the desired tunability needed to observe unconventional superconductivity at the edge of magnetism.

VI. ACKNOWLEDGEMENTS

We thank Qimiao Si and Alannah Hallas for useful discussions, and Ashifia Huq for help with POWGEN beam-line experiments. KB, CLH, and EM acknowledge support from the Gordon and Betty Moore Foundation

through EPiQS initiative grant GBMF 4417, with partial support for KB from the National Science Foundation Grant No. DMR-1506704. Work at IQM was supported by the U.S. Department of Energy, Office of Basic Energy Sciences, Division of Material Sciences and Engineering under Grant No. DE-FG02-08ER46544. AHN and VL acknowledge the support of the Robert A. Welch Foundation Grant No. C-1818. AHN was also supported by the National Science Foundation Grant No. DMR-1350237. Computational resources at Rice University were provided by the Big-Data Private-Cloud Research Cyberinfrastructure MRI-award funded by the NSF under Grant No. CNS-1338099. Work at Oak Ridge National Laboratory's Spallation Neutron Source was sponsored by the Scientific User Facilities Division, Office of Basic Energy Sciences, U.S. Department of Energy.
